Electronic Supplementary Material (ESI) for Journal of Materials Chemistry A.

Direct Evidence for High Na^+ Mobility and High Voltage Structural Processes in P2-$Na_x[Li_yNi_zMn_{1-y-z}]O_2$ ($x,y,z \leq 1$) Cathodes from ^{23}Na and ^{7}Li Solid-State NMR and First Principles Density Functional Theory Calculations

Supplementary Information

R. J. Clément,[a,b] J. Xu,[c,d] D. S. Middlemiss,[a,e] J. Alvarado,[c] C. Ma,[c] Y. S. Meng,[c] C. P. Grey[a]

[a] Department of Chemistry, University of Cambridge, Cambridge, CB2 1EW, UK.

[b] Current address: Department of Materials Science and Engineering, University of California Berkeley, Berkeley, CA 94705, USA.

[c] Department of NanoEngineering, University of California San Diego, La Jolla, CA 92037, USA.

[d] Department of Materials Science and Engineering, Iowa State University, Ames, IA 50011, USA.

[e] Department of Chemistry, University of Warwick, Coventry, CV4 7AL, UK.

1. Additional *ex situ* solid-state NMR and X-ray diffraction data

1.1. High field ^{23}Na ssNMR data on as–synthesized P2-$Na_{2/3}Ni_{1/3}Mn_{2/3}O_2$

The spectra acquired at a field of 16.44 T on as-synthesized P2-$Na_{2/3}Ni_{1/3}Mn_{2/3}O_2$ reveal the presence of two Na environments in the sample, as shown in Figure S1 and in good agreement with a recent report.[1]

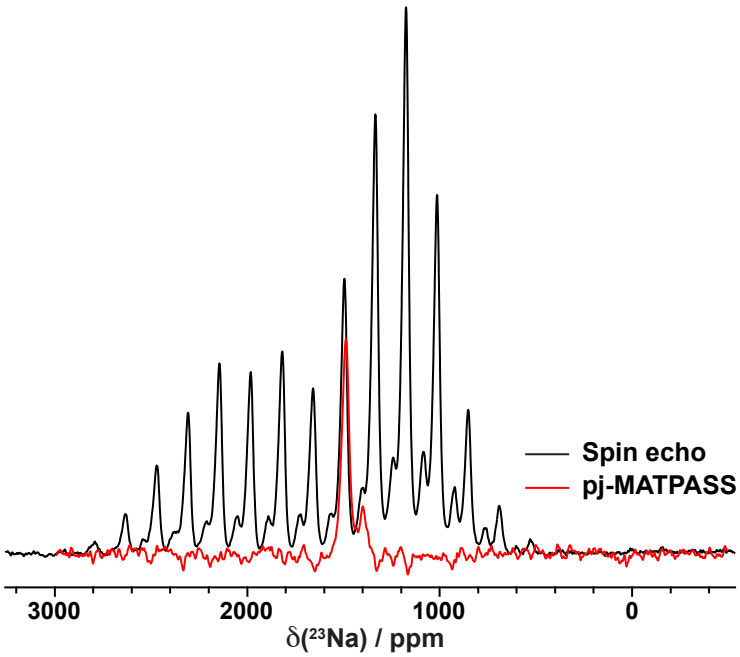

Figure S1. ^{23}Na NMR on as-synthesized P2-$Na_{2/3}Ni_{1/3}Mn_{2/3}O_2$ at 30 kHz MAS and at an external field of 16.44 T. The sample temperature is 328.2 K (55.1 °C). A spin echo spectrum is overlaid with a pj-MATPASS isotropic spectrum. In the latter, spinning sidebands are suppressed and peaks are observed at the resonant frequencies of the different Na environments in the sample.[2]

The major Na environment in the spectrum shown above can be fitted with an isotropic shift δ_{iso} = 1511 ppm, a hyperfine dipolar anisotropy $\Delta_\delta = \delta_{ZZ} - \frac{1}{2}(\delta_{XX} + \delta_{YY})$ of 1049 ppm, and a quadrupolar constant C_Q of 3.6 MHz. The δ_{iso} and C_Q parameters are approximately halfway between the values computed from first principles for the edge- (P(2d)) and face-centered (P(2b)) sites in the P2-$Na_{2/3}Ni_{1/3}Mn_{2/3}O_2$ structure (structural diagrams for the different Na environments are shown in Figure 4, and the computed NMR parameters are presented in Table 1 in the main text), and the experimental Δ_δ parameter is a

lot smaller than those computed from first principles. These observations suggest that Na^+ ion exchange between the different prismatic sites in the P2 layers is fast on the NMR timescale and results in coalescence of the P(2b) and P(2d) resonances and in a reduced Δ_δ. The major Na environment is assigned to the resulting average P2 signal.

The minor Na environment can be fitted with δ_{iso} = 1422 ppm, Δ_δ = 1075 ppm, and C_Q = 4.4 MHz. Yang and coworkers assigned this resonance to a sodium-poor phase with x < 0.66 formed upon exposure to moisture.[1] Yet, a previous study showed that the as-prepared phase is not prone to water intercalation,[3] and our pristine powder sample was dried in a vacuum oven overnight at 100°C and packed in the glovebox prior to the NMR measurements. For these reasons, and because the minor Na environment can be fitted with NMR parameters close to those obtained from first principles for an octahedral (O_h) site in O2-$Na_{2/3}Ni_{1/3}Mn_{2/3}O_2$ (see Table 1 in the main text), we assign this signal to O_h Na in O2-type stacking faults in the major P2 phase, noting that O2-type stacking faults have also been observed in as-synthesized P2-$Na_{0.8}Li_{0.12}Ni_{0.22}Mn_{0.66}O_2$.[4]

1.2. Fits of selected ^{23}Na NMR spectra collected during the first electrochemical cycle of P2-$Na_{2/3}Ni_{1/3}Mn_{2/3}O_2$ at 4.7 T

As shown in Figure S2, a good fit of the ^{23}Na NMR spectrum collected at 3.4 V discharge (x_{Na} = 0.41) is obtained when the two major resonances observed at 3.4 and 3.7 V (at x_{Na} = 0.52 and 0.36, respectively) charge are superimposed.

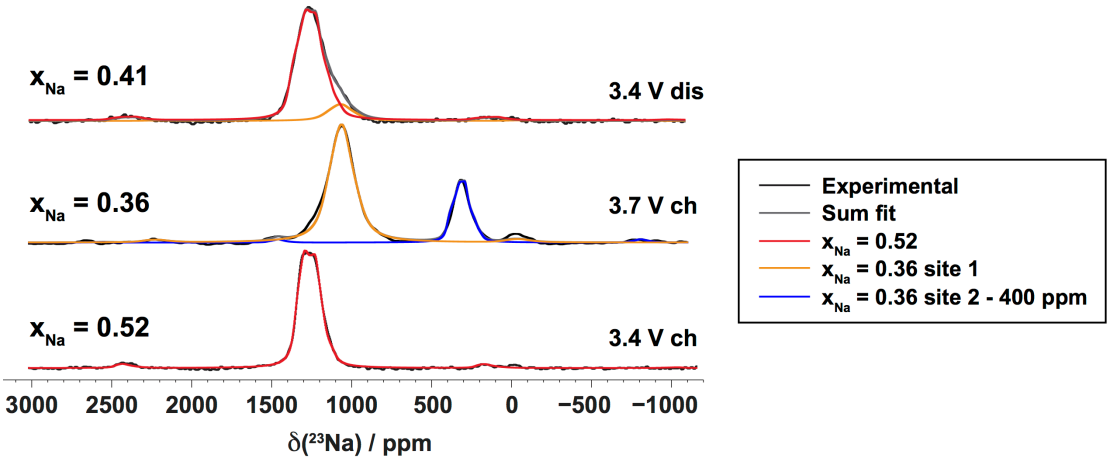

Figure S2. Fitted ^{23}Na NMR spectra collected on various samples obtained between 3.4 and 3.7 V upon first charge and first discharge of the P2-$Na_{2/3}Ni_{1/3}Mn_{2/3}O_2$ cathode.

1.3. Investigation of the hygroscopic character of the P2-$Na_xLi_{0.12}Ni_{0.22}Mn_{0.66}O_2$ cathode at high voltage

1.3.a. ^{1}H ssNMR data on 4.4 V charged P2-$Na_xLi_{0.12}Ni_{0.22}Mn_{0.66}O_2$ at 4.7 T

^{1}H ssNMR data collected on a 4.4 V charged P2-$Na_xLi_{0.12}Ni_{0.22}Mn_{0.66}O_2$ sample (sample #2) at 4.7 T are shown in Figure S3.

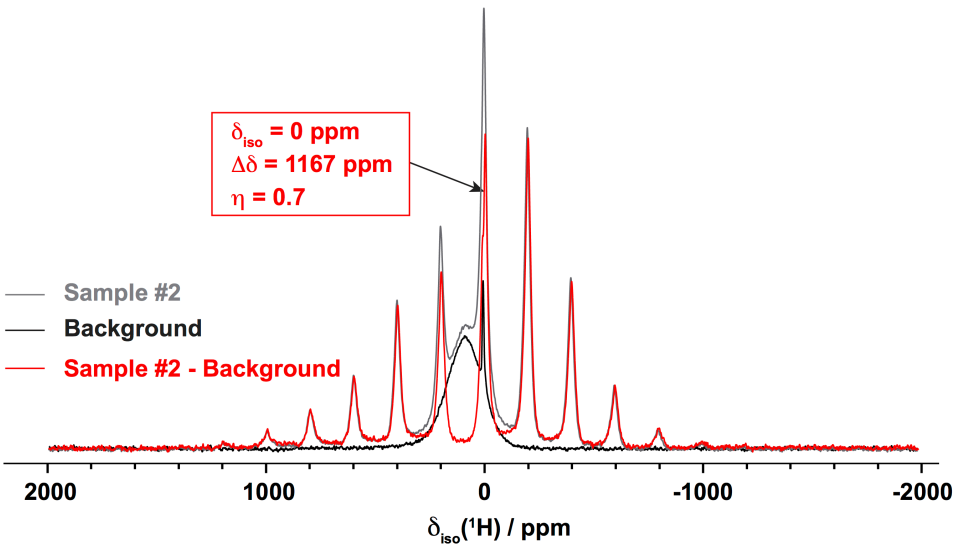

Figure S3. Room temperature ^{1}H spectrum obtained for the P2-$Na_xLi_{0.12}Ni_{0.22}Mn_{0.66}O_2$ sample #2 charged to 4.4 V. The data were acquired at 4.7 T (at a Larmor frequency of -200.1 MHz) using a double-resonance 1.3 mm HX probe, under 40 kHz MAS. The ^{1}H chemical shift was referenced against adamantane (δ_{iso} = 1.87 ppm). The ^{1}H spin echo NMR spectrum was acquired using a 90° RF pulse of 0.75 μs and a 180° RF pulse of 1.5 μs at 64 W, and a recycle delay of 10 ms. The NMR probe background signal (black) was subtracted from the original spectrum (grey) to isolate the signal arising from the cathode (red). The NMR parameters obtained from a fit of the resulting ^{1}H signal are shown on the spectrum: the isotropic shift (δ_{iso}), the dipolar anisotropy (Δ_δ), and the dipolar asymmetry (η).

1.3.b. Ex situ X-ray diffraction data obtained on a 4.4 V charged P2-$Na_xLi_{0.12}Ni_{0.22}Mn_{0.66}O_2$ sample

The effect of sample aging on the long-range structure of the 4.4 V charged P2-$Na_xLi_{0.12}Ni_{0.22}Mn_{0.66}O_2$ cathode was studied with *ex situ* X-ray diffraction (XRD). An electrochemical cell was charged to 4.4 V, opened and disassembled in an Ar-filled glovebox

and the $Na_xLi_{0.12}Ni_{0.22}Mn_{0.66}O_2$ cathode sample was mounted on an XRD sample holder and covered with Kapton tape to avoid air/moisture exposure. An XRD scan was recorded a few hours after cycling (fresh data). The sample was then left in the XRD sample holder to age in air. The Kapton tape was not removed. A second XRD scan (aged data) was recorded two days after cycling. The two diffraction patterns (denoted as 'fresh' and 'aged') are shown in Figure S4.

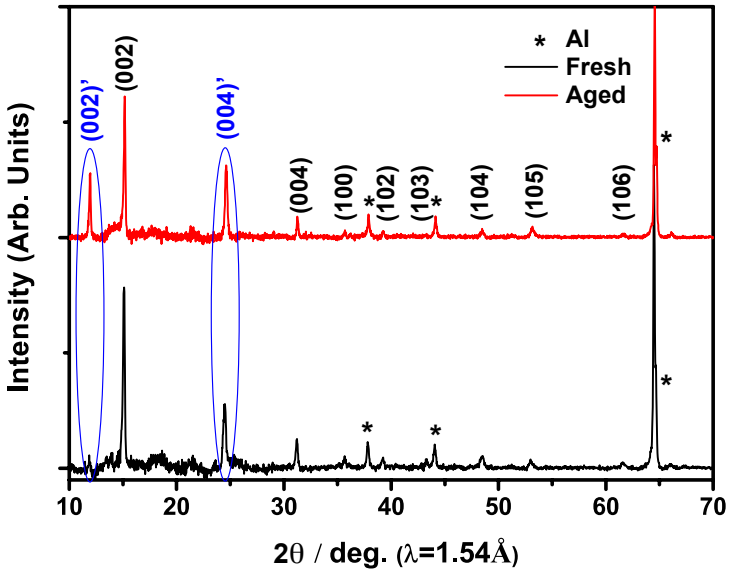

Figure S4. *Ex situ* XRD patterns collected on a P2-$Na_xLi_{0.12}Ni_{0.22}Mn_{0.66}O_2$ sample charged to 4.4 V: freshly cycled (fresh), and two days after cycling (aged). The peaks due to the aluminum current collector are indicated by an asterisk. The reflections due to the hydrated phase are labelled in blue.

All major reflections of the water-free P2 phase are clearly present in the fresh and aged patterns, indicating that the P2 framework is maintained up to 4.4 V charge. An additional reflection at ca. 24.6° in 2θ, similar to the (004)' reflection observed for the hydrated P2-$Na_{0.34}Ni_{0.22}Co_{0.11}Mn_{0.66}O_2$[5] and P2-$Na_{0.6}MnO_2$[6] phases, is present in the fresh *ex situ* pattern and suggests that water molecules quickly intercalate into some of the partially desodiated P2 layers. In the aged pattern, the (004)' peak is more intense and the (002)' reflection assigned to the hydrated phase[3,5,6] appears at ca. 12.0°, indicating more extensive water uptake over time. The positions of the 2θ reflections suggest an interlayer spacing *c* comprised between 14.4 and 14.7 Å for the water-intercalated P2 layers. The fact that the (004)' reflection is more intense and appears before the (002)' reflection may also result from overlap between two reflections at ca. 24.6°.

2. First principles calculations of magnetic exchange couplings and ^{7}Li and ^{23}Na NMR parameters

2.1. Additional computational details for the CRYSTAL09 calculations

All-electron atom-centered basis sets comprising fixed contractions of Gaussian primitive functions were employed throughout. Two spin-polarized exchange-correlation functionals based upon the B3LYP form,[7-10] and with Fock exchange weights of F_0 = 20 % (B3LYP or H20) and 35 % (H35) were chosen for their good performance for the electronic structure and band gaps of transition metal compounds (B3LYP or H20),[11,12] and for their accurate description of the magnetic properties of related compounds (H35).[13-15] Besides, previous studies have shown that the hyperfine shifts calculated with the H20 and the H35 functionals on similar compounds are in good agreement with experiment.[16-18] Two types of basis sets were used: a smaller basis set (BS-I) was employed for structural optimizations, and a larger basis set (BS-II) was used for computing magnetic coupling constants and NMR parameters which require an accurate description of the occupation of core-like electronic states. For BS-I, individual atomic sets are of the form (7s2p1d)/[1s2sp1d] for Li, (15s7p)/[1s3sp] for Na, (20s12p5d)/[1s4sp2d] for Ni and Mn, and (14s6p1d)/[1s3sp1d] for O, where the values in parentheses denote the number of Gaussian primitives and the values in square brackets the contraction scheme. All BS–I sets were obtained from the CRYSTAL online repository and were unmodified from their previous use in a broad range of compounds.[19] For BS-II, a modified IGLO-III (10s6p2d)/[6s5p2d] set was adopted for O, flexible and extended TZDP-derived (9s2p)/[5s2p] and (11s7p)/[7s3p] sets were used for Li and Na, respectively, and an Ahlrichs DZP-derived (13s9p5d)/[7s5p3d] set was applied to Ni and Mn.[20]

NMR parameters were computed in fully optimized (atomic positions and cell parameters) P2- and O2-type $Na_{2/3}Ni_{1/3}Mn_{2/3}O_2$, P2-$Na_{1/3}Ni_{1/3}Mn_{2/3}O_2$ and P2-$Na_{0.83}Li_{0.16}Ni_{0.16}Mn_{0.67}O_2$. Magnetic coupling constants were computed in the optimized P2 structures. All first principles structural optimizations were carried out in the ferromagnetic (FM) state, after removal of all symmetry constraints (within the P1 space group), and using the H20 hybrid functional. 24 formula unit supercells were used throughout. Structural optimizations were pursued using the quasi-Newton algorithm with RMS convergence tolerances of 10^{-7}, 0.0003, and 0.0012 au for total energy, root-mean-square (rms) force, and rms displacement, respectively. Tolerances for maximum force and displacement components were set to 1.5 times the respective rms values. Sufficient convergence in total energies and spin densities was obtained by application of integral series truncation thresholds of 10^{-7}, 10^{-7},

10^{-7}, 10^{-7}, and 10^{-14} for Coulomb overlap and penetration, exchange overlap, and g- and n-series exchange penetration, respectively, as defined in the CRYSTAL documentation.[19] The final total energies and spin and charge distributions were obtained in the absence of any spin and eigenvalue constraints. NMR parameters were obtained on ferromagnetically aligned supercells, and on supercells in which one (Mn or Ni) spin was flipped, using BS-II sets and a method identical to that described in Middlemiss et al.'s recent work.[17] Isotropic Monkhorst-Pack[21] reciprocal space meshes with shrinking factor 4 were used throughout.

2.2. First principles magnetic exchange couplings in $Na_x[Li_yNi_zMn_{1-y-z}]O_2$ compounds

2.2.a. Methodology

Magnetic exchange constants (J_a) were evaluated from the first principles energy difference between the purely ferromagnetic cell (E_{ferro}) and carefully selected sets of spin configurations wherein individual and pairs of Mn spins were flipped (E_{mag}),

$$E_{\mathrm{mag}} - E_{\mathrm{ferro}} = 2\sum_{a} J_a \sum_{i,j\in a} S_i S_j \qquad \text{(S1)},$$

where the sum is made over all i,j spin pairs with formal spins S_i and S_j, in antiferromagnetic configurations for each interaction type, without double counting. The factor of 2 is present because the energy is defined relative to the purely ferromagnetic state. This results in a set of linear equations that were solved simultaneously to yield the different J_a values. Within the sign convention applied here, positive J_a values correspond to ferromagnetic interactions between the spins, while negative J_a values correspond to antiferromagnetic interactions.

2.2.b. First principles exchange couplings in $P2\text{-}Na_{2/3}Ni_{1/3}Mn_{2/3}O_2$ and $P2\text{-}Na_{0.83}Li_{0.16}Ni_{0.16}Mn_{0.67}O_2$

Eight magnetic coupling interactions between nearest neighbour Mn and Ni spins were considered in the magnetic Monte Carlo simulations. The six in-plane magnetic exchange interactions examined in this work are depicted in Figure S5.

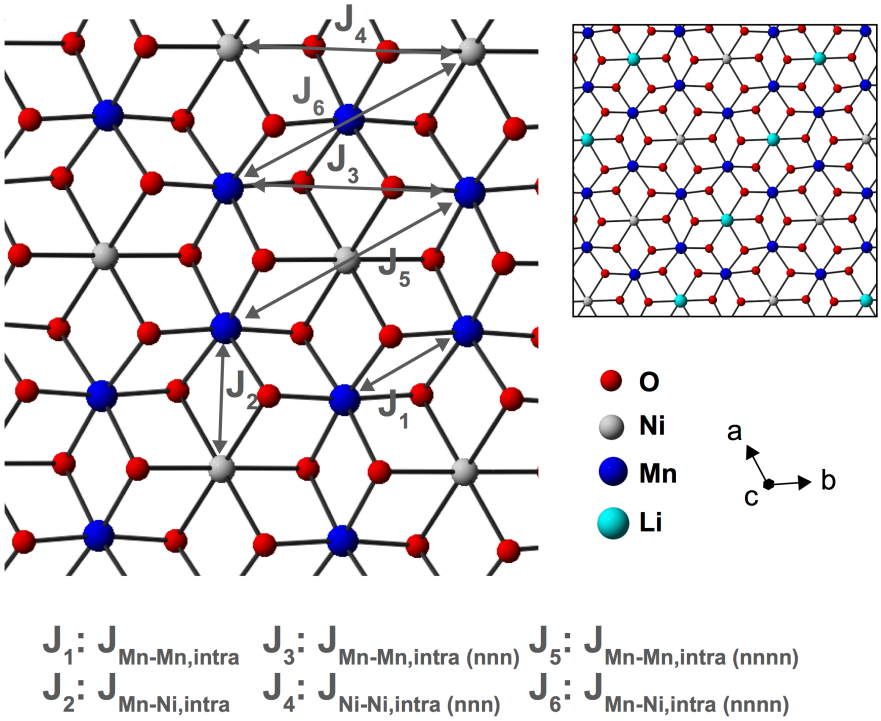

Figure S5. In-plane magnetic exchange interactions (J_a couplings, a = 1…6) in honeycomb ordered $Na_xNi_{1/3}Mn_{2/3}O_2$ superstructures. The metal lattice in $Na_xLi_{0.16}Ni_{0.16}Mn_{0.67}O_2$ is shown in the inset. J_a interactions in $Na_xLi_{0.16}Ni_{0.16}Mn_{0.67}O_2$ are similar to those depicted for $Na_xNi_{1/3}Mn_{2/3}O_2$, save that in the former compound half of the Ni ions are replaced by non-magnetic Li ions.

The coupling constants computed in the optimized P2-$Na_{2/3}Ni_{1/3}Mn_{2/3}O_2$ and P2-$Na_{0.83}Li_{0.16}Ni_{0.16}Mn_{0.67}O_2$ structures are presented in Tables S1a and S1b.

a) P2-$Na_{2/3}Ni_{1/3}Mn_{2/3}O_2$			
J / K	HYB20	HYB35	d(TM-TM) and TM-O-TM angle
$J_{\mathrm{Mn-Mn,intra}}$	-18.94	-19.08	2.84 Å, 2 x 98°
$J_{\mathrm{Mn-Ni,intra}}$	-35.29	-13.54	2.84 Å, 92 and 93°
$J_{\mathrm{Mn-Mn,inter}}$	-0.62	-0.46	5.45 Å
$J_{\mathrm{Mn-Ni,inter}}$	0.34	0.09	5.40 Å
$J_{\mathrm{Mn-Mn,intra}}\ (nnn)$	0.88	1.24	4.93 Å
$J_{\mathrm{Ni-Ni,intra}}\ (nnn)$	0.15	0.03	4.91 Å
$J_{\mathrm{Mn-Mn,intra}}\ (nnnn)$	-1.71	-1.01	5.67 Å
$J_{\mathrm{Mn-Ni,intra}}\ (nnnn)$	7.66	5.49	5.69 Å

b) P2-$Na_{0.83}Li_{0.16}Ni_{0.16}Mn_{0.67}O_2$			
J / K	H20	H35	d(TM-TM) and TM-O-TM angle
$J_{\mathrm{Mn-Mn,intra}}$	-26.50	-24.87	2.79 Å, 97 and 98°
$J_{\mathrm{Mn-Ni,intra}}$	-27.97	-9.34	2.93 Å, 93 and 94°
$J_{\mathrm{Mn-Mn,inter}}$	-0.96	-0.70	5.42 Å
$J_{\mathrm{Mn-Ni,inter}}$	0.66	0.46	5.42 Å
$J_{\mathrm{Mn-Mn,intra}}\ (nnn)$	1.72	1.75	4.90 Å
$J_{\mathrm{Ni-Ni,intra}}\ (nnn)$	0.27	0.10	4.99 Å
$J_{\mathrm{Mn-Mn,intra}}\ (nnnn)$	-1.55	-0.92	5.69 Å
$J_{\mathrm{Mn-Ni,intra}}\ (nnnn)$	7.34	5.15	5.77 Å

Table S1. First principles coupling constants obtained in a) P2-$Na_{2/3}Ni_{1/3}Mn_{2/3}O_2$ and b) P2-$Na_{0.83}Li_{0.16}Ni_{0.16}Mn_{0.67}O_2$, using H20 and H35 functionals. In these and in Table S2, TM-TM distances and bond angles (for superexchange interactions) are recorded.

Large differences are observed between the nearest-neighbour in-plane Mn-Ni interactions computed in P2-$Na_{2/3}Ni_{1/3}Mn_{2/3}O_2$ and P2-$Na_{0.83}Li_{0.16}Ni_{0.16}Mn_{0.67}O_2$, but also between the magnetic couplings obtained using H20 and H35 functionals.

The competing magnetic interactions between neighbouring metal spins in these materials are presented in Figure S6. The top two diagrams depict the interactions between neighboring Mn spins in the TM layers. In the top left diagram, the exchange interaction between two half-filled Mn t_{2g} orbitals, resulting from direct orbital overlap, leads to antiferromagnetic spin alignment and decreases sharply with Mn-Mn distance. In the top right diagram, the approximately 90° Mn-O-Mn superexchange interaction between the two Mn t_{2g} orbitals occurs via two orthogonal (filled) p orbitals on O and leads to ferromagnetic alignment of the spins. The sign and magnitude of the overall $J_{\mathrm{Mn-Mn,intra}}$ coupling depends on the relative strength of the two competing interactions described above. In P2-$Na_{2/3}Ni_{1/3}Mn_{2/3}O_2$ and P2-$Na_{0.83}Li_{0.16}Ni_{0.16}Mn_{0.67}O_2$, the Mn-Mn distances are short and antiferromagnetic direct exchange dominates.

The bottom two diagrams depict the interactions between neighboring Mn and Ni spins in the TM layers. In the bottom left diagram, the 90° superexchange Ni-O-Mn interaction between the Ni e_g and Mn t_{2g} half-filled orbitals, via a single (filled) p orbital on O, leads to antiferromagnetic alignment of the spins. When two such 90° superexchange interactions are considered, as shown in the bottom right diagram, overlap between the Ni e_g orbital and the two O p orbitals lead to one in-phase and one out-of-phase interaction with the Mn t_{2g} orbital. In this case, net ferromagnetic alignment of the spins is observed. The first

principles $J_{\mathrm{Mn-Ni,intra}}$ values obtained in P2-$Na_{2/3}Ni_{1/3}Mn_{2/3}O_2$ and P2-$Na_{0.83}Li_{0.16}Ni_{0.16}Mn_{0.67}O_2$ indicate that the net interaction is antiferromagnetic and is stronger in P2-$Na_{2/3}Ni_{1/3}Mn_{2/3}O_2$ than in P2-$Na_{0.83}Li_{0.16}Ni_{0.16}Mn_{0.67}O_2$.

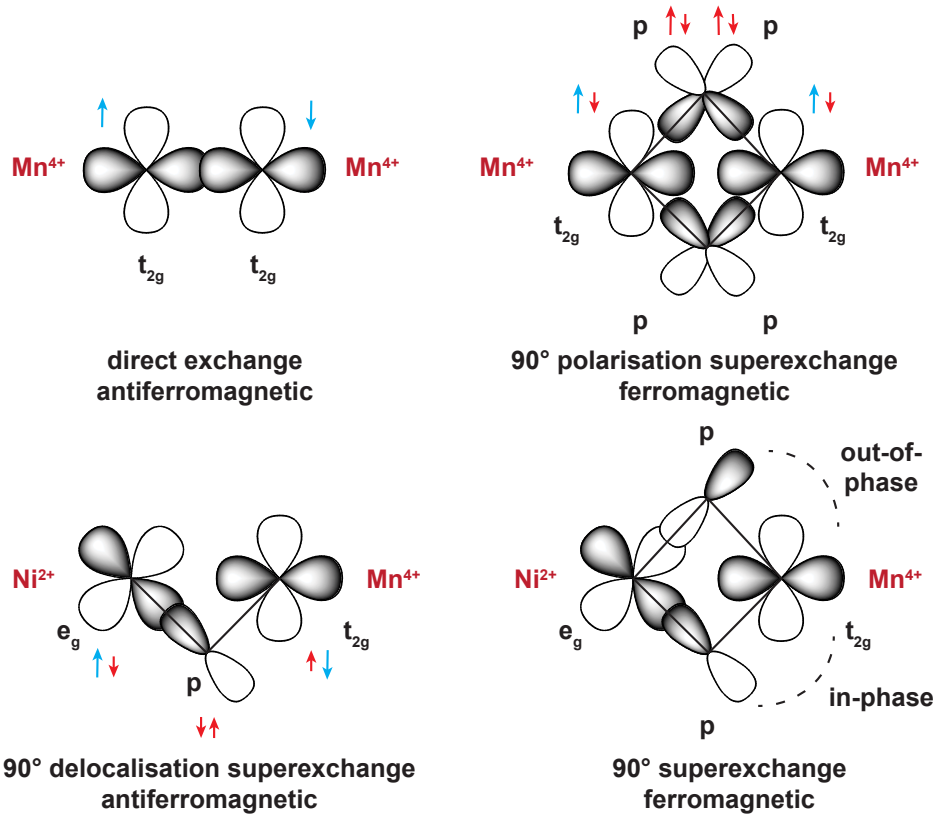

Figure S6. Competing magnetic interactions between nearest-neighbor Mn and Ni spins.

The differences between the coupling constants computed in $Na_x[Li_yNi_zMn_{1-y-z}]O_2$ structures using the H20 and H35 functionals presumably arise from the changing nature of the electronic states at the Fermi level when more HF exchange is included in the exchange correlation functional. In NiO, Corà et al. reported that the filled Ni 3d band is progressively shifted to higher energy on decreasing the proportion of exact exchange in the functional. Between 20 and 30% Fock exchange, the Ni 3d band becomes higher than the O 2p band.[11] A similar raise in the energy of the Ni 3d band is observed in the density of states (DOS) plots for P2-$Na_{2/3}Ni_{1/3}Mn_{2/3}O_2$ (shown in Figure S7) and for P2-$Na_{0.83}Li_{0.16}Ni_{0.16}Mn_{0.67}O_2$, when going from H35 to H20. For both compounds, the proportion of Ni 3d states at the Fermi level is greater and the nearest-neighbor Mn-Ni exchange interactions are approximately three times larger (see Tables S1a and S1b) when using H20 than when using H35.

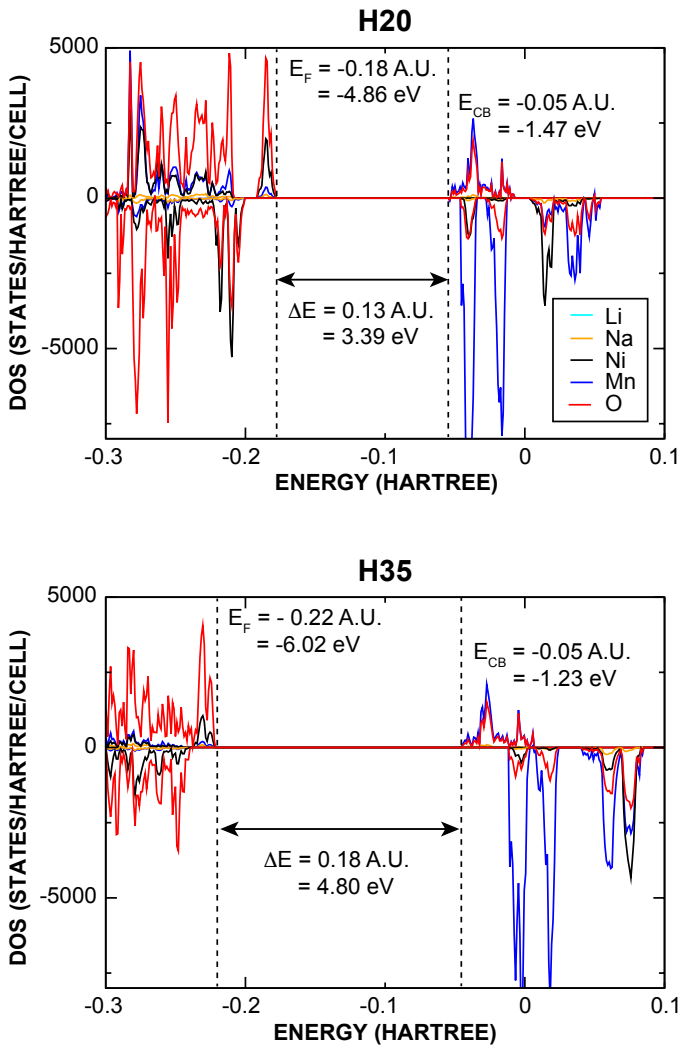

Figure S7. Density of states (DOS) plots for P2-$Na_{2/3}Ni_{1/3}Mn_{2/3}O_2$, computed from the final H20 and H35 electronic wavefunctions used to calculate the magnetic couplings and NMR parameters. E_F, E_{CB}, and ΔE stand for the Fermi energy (HOMO energy), the lowest energy of the conduction band (LUMO), and the band gap, respectively.

2.2.c. First principles exchange couplings in P2-$Na_{1/3}Ni_{1/3}Mn_{2/3}O_2$

The coupling constants computed in the optimized P2-$Na_{1/3}Ni_{1/3}Mn_{2/3}O_2$ structure are shown in Table S2. The presence of Jahn-Teller active Ni^{3+} ions in P2-$Na_{1/3}Ni_{1/3}Mn_{2/3}O_2$ leads to a local distortion of the NiO_6 octahedra. Two long (L) Ni-O bonds (d(Ni-O) = 2.10 Å) are present along the Jahn-Teller axis, and four short (S) Ni-O bonds (d(Ni-O) = 1.90 Å) are observed in the other directions. MnO_6 octahedra are also slightly distorted, with two shorter (S) Mn-O bonds (d(Mn-O) = 1.85 Å) and four longer (L) Mn-O bonds (d(Mn-O) = 1.90-1.91 Å). Each Mn in the lattice interacts with three nn Ni via a double 90° J_2 interaction (see

Figure S5): two of these interactions proceed via one short and one long Ni-O bond (SL), and one proceeds via two short Ni-O bonds (SS). Each Mn in the lattice also interacts with three nearest-neighbor Mn via a double 90° J_1 interactions (see Figure S5): two of these interactions proceed via long Mn-O bonds (LL), and one proceeds via short Mn-O bonds (SS).

J / K	H20	H35	d(TM-TM) and TM-O-TM angle
$J_{\mathrm{Mn-Mn,intra}}$	-27.31#	-26.43#	2.88 Å, 2 x 98.2° (LL) 2.77 Å, 2 x 96.6° (SS)
$J_{\mathrm{Mn-Ni,intra}}$	-16.71#	-7.47#	2.85 Å, 97.4 and 92.1° (SL) 2.82 Å, 2 x 95.4° (SS)
$J_{\mathrm{Mn-Mn,inter}}$	-0.30	-0.20	5.73 Å
$J_{\mathrm{Mn-Mn,intra}}\ (nnn)$	1.71	1.44	4.89 Å
$J_{\mathrm{Ni-Ni,intra}}\ (nnn)$	1.50	1.62	4.88 Å
$J_{\mathrm{Mn-Mn,intra}}\ (nnnn)$	-6.62	-3.75	5.71 Å
$J_{\mathrm{Mn-Ni,intra}}\ (nnnn)$	2.85	1.62	5.58 Å

Table S2. First principles coupling constants obtained in P2-$Na_{1/3}Ni_{1/3}Mn_{2/3}O_2$ using H20 and H35 functionals. The distortion of the NiO_6 octahedra in the P2-$Na_{1/3}Ni_{1/3}Mn_{2/3}O_2$ structure leads to anisotropic nearest-neighbor Ni-Mn and Mn-Mn interactions. SS, SL, and LL indicate nearest-neighbor interactions proceeding via two short, one short one long, and two long TM-O bonds, respectively. Axially averaged magnetic couplings are indicated with #.

The absence of a long-range structural distortion in P2-$Na_{1/3}Ni_{1/3}Mn_{2/3}O_2$ suggests that Ni^{3+} Jahn-Teller distortions are local rather than cooperative. As in related $LiNi_xCo_{1-x}O_2$ materials, a dynamic Jahn-Teller effect, whereby the distortion around the Ni^{3+} ions fluctuates over the three directions of space, is expected at room temperature.[17] Hence, the $J_{\mathrm{Mn-Mn,intra}}$ and $J_{\mathrm{Mn-Ni,intra}}$ couplings shown in Table S2 have been axially averaged:

$$J_{\mathrm{Mn-Mn,intra}} = \frac{J_{1,SS} + 2J_{1,LL}}{3} \quad \text{(S2)},$$

and

$$J_{\mathrm{Mn-Ni,intra}} = \frac{J_{2,SS} + 2J_{2,SL}}{3} \quad \text{(S3)}.$$

2.3. Site-specific Ni and Mn magnetic scaling factors in $Na_x[Li_yNi_zMn_{1-y-z}]O_2$ compounds derived from Monte Carlo simulations

2.3.a. Methodology and Computational details

The code implements an Ising-type magnetic model for ions with spins, S, quantized in the direction of the external magnetic field, B_0, with spin magnetic moments $M_S = -S, -S+1 \ldots S-1, S$. The Hamiltonian is of the form:

$$H = -\mu B_0 \sum_i M_S - \frac{1}{2} \sum_{<i,j>} J_a M_S^i M_S^j \qquad \text{(S4)},$$

where the first sum describes the interaction with the external magnetic field and the second sum accounts for the internal magnetic interactions between neighboring spins. J_a is the magnetic exchange energy between the ij ion pair and the factor of 1/2 compensates for double counting. The J_a magnetic constants (see Figure S5) were obtained from hybrid HF/DFT calculations using the CRYSTAL09 code, as described earlier. The Monte Carlo simulations were performed on (4*a*, 3*b*, 3*c*) expansions of the P2-$Na_xNi_{1/3}Mn_{2/3}O_2$ (x = 2/3, 1/3) and P2-$Na_{0.83}Li_{0.16}Ni_{0.16}Mn_{0.67}O_2$ superstructures used for NMR calculations. The P2-$Na_xNi_{1/3}Mn_{2/3}O_2$ (x = 2/3, 1/3) and P2-$Na_{0.83}Li_{0.16}Ni_{0.16}Mn_{0.67}O_2$ Monte Carlo cells contained 864 and 720 transition metal spins, respectively. The simulations were initiated in an antiferromagnetic configuration at 400 K and the temperature of the heat bath was subsequently decreased in steps of 10 K, down to 320 K. An external magnetic field of 4.7 T was applied. The Metropolis algorithm was used to sample the spin configurational space and allow the system to equilibrate with the heat bath through a series of random single spin flips. After 100 k initialization steps, 800 k Monte Carlo steps were performed at each temperature step, and the cumulative spin configurations were saved every 100 k steps. The number of spin flips per Monte Carlo step was set to ten times the number of Mn spins in the supercell. The final spin configuration at temperature T served as the starting configuration for the following temperature step at T'=T-10 K.

2.3.b. Results

Separate Monte Carlo simulations were performed using each of the eight sets of coupling constants presented in Tables S1a, S1b, and S2, as computed in the optimized P2-$Na_{2/3}Ni_{1/3}Mn_{2/3}O_2$, P2-$Na_{0.83}Li_{0.16}Ni_{0.16}Mn_{0.67}O_2$, and P2-$Na_{1/3}Ni_{1/3}Mn_{2/3}O_2$ structures,

respectively, using H20 and H35 functionals. Site-specific scaling factors at 320 K, for inequivalent Ni and Mn sites in the various structures, are shown in Tables S3a, S3b, and S3c, and were obtained from the magnetic moments at individual sites averaged over all Monte Carlo iterations:

$$\Phi_i(320\ \mathrm{K}) = \frac{\langle M_{\mathrm{MC}}(320\ \mathrm{K})\rangle_i}{M_{\mathrm{sat}}} \quad \text{(S5)},$$

where $\langle M_{\mathrm{MC}}(320\ \mathrm{K})\rangle_i$ is the average magnetic moment for metal site i at 320 K, and M_{sat} is the saturation magnetic moment for the transition metal species occupying site i.

Interlayer magnetic interactions have a negligible effect on the magnetic moments at the Mn sites, as demonstrated by the similar scaling factors obtained e.g. for Mn_A and Mn_B in P2-$Na_{2/3}Ni_{1/3}Mn_{2/3}O_2$. The Ni^{2+} scaling factors obtained using H20 magnetic couplings are lower than those computed using H35 values (see Tables S3a and S3c), presumably because of the very different $J_{\mathrm{Mn-Ni,intra}}$ couplings determined with the two functionals (see Tables S1a and S1b).

a) P2-$Na_{2/3}Ni_{1/3}Mn_{2/3}O_2$				
Scaling factor	Intralayer interactions	Interlayer interactions	Φ(H20)	Φ(H35)
Φ_{MnA}	3 Ni, 3 Mn nn, 6 Mn nnn	2 Mn	1.19×10^{-2}	1.27×10^{-2}
Φ_{MnB}		2 Ni	1.20×10^{-2}	1.28×10^{-2}
$\Phi_{Ni(II)}$	6 Mn nn, 6 Ni nnn	2 Mn	6.77×10^{-3}	1.11×10^{-2}
Average Φ			1.02×10^{-2}	1.22×10^{-2}

b) P2-$Na_{1/3}Ni_{1/3}Mn_{2/3}O_2$				
Scaling factor	Intralayer interactions	Interlayer interactions	Φ(H20)	Φ(H35)
Φ_{MnA}	3 Ni, 3 Mn nn, 6 Mn nnn	2 Mn	1.15×10^{-2}	1.20×10^{-2}
Φ_{MnB}		2 Ni	1.16×10^{-2}	1.20×10^{-2}
$\Phi_{Ni(III)}$	6 Mn nn, 6 Ni nnn	2 Mn	3.82×10^{-3}	4.48×10^{-3}
Average Φ			8.98×10^{-3}	9.49×10^{-3}

c) P2-$Na_{0.83}Li_{0.16}Ni_{0.16}Mn_{0.67}O_2$				
Scaling factor	Intralayer interactions	Interlayer interactions	**Φ**(H20)	**Φ**(H35)
Φ_{MnA1}	1 Ni, 2 Li, and 3 Mn nn, and 3 Ni, 3 Mn nnn	2 Mn	1.24×10^{-2}	1.29×10^{-2}
Φ_{MnA2}		2 Ni	1.26×10^{-2}	1.31×10^{-2}
Φ_{MnB1}	2 Ni, 1 Li, and 3 Mn nn, and 3 Li, 3 Mn nnn	2 Mn	1.12×10^{-2}	1.22×10^{-2}
Φ_{MnB2}		2 Li	1.13×10^{-2}	1.22×10^{-2}
$\Phi_{Ni(II)}$	6 Mn nn, and 4 Li, 2 Ni nnn	2 Mn	8.63×10^{-3}	1.22×10^{-2}
Average **Φ**			1.12×10^{-2}	1.25×10^{-2}

Table S3. Ni and Mn site-specific scaling factors obtained in the honeycomb-ordered a) P2-$Na_{2/3}Ni_{1/3}Mn_{2/3}O_2$, b) P2-$Na_{1/3}Ni_{1/3}Mn_{2/3}O_2$, and c) P2-$Na_{0.83}Li_{0.16}Ni_{0.16}Mn_{0.67}O_2$ superstructures. Site-specific scaling factors were determined at 320 K and at an external field of 4.7 T. The 'average **Φ**' corresponds to the weighted average scaling factor when all metal sites in the structure are considered.

We note that the isotropic shifts for the various Na sites in P2-$Na_{2/3}Ni_{1/3}Mn_{2/3}O_2$ obtained directly from the computed nuclear spin density scaled by the average scaling factor **Φ** shown in Table S3a (underestimating the Mn contributions and overestimating the Ni contributions), and the reconstructed isotropic shifts determined from the sum of the TM-O-Na bond pathway contributions scaled by the site-specific scaling factors shown in Table S3a, are in good agreement. These two sets of shifts are presented in Tables 1 and 2 in the main text.

An experimental bulk scaling factor of $\Phi(320\text{ K}) = 1.02\times10^{-2}$ was derived from the experimental molar magnetic susceptibility of P2-$Na_{2/3}Ni_{1/3}Mn_{2/3}O_2$ ($\chi_m(320K) = 3.40\times10^{-3}$ emu.mol^{-1}), using an expression similar to that derived by Kim et al.[16]:

$$\Phi(T) = \frac{B_0\chi_m(T)}{g_e\mu_B S N_A}\left(\frac{\mu_{eff,exp}}{\mu_{eff,so}}\right)^2 \quad \text{(S6)},$$

where B_0 if the external magnetic field, g_e is the electron g-factor, μ_B is the Bohr magneton, S is the average TM spin, N_A is Avogadro's number, $\mu_{eff,exp}$ is the experimental effective

magnetic moment, and $\mu_{eff,so}$ the spin only value ($\mu_{eff,so} = 2\sqrt{S(S+1)}$). The factor $(\frac{\mu_{eff,exp}}{\mu_{eff,so}})^2$ corrects for spin-orbit coupling and/or zero field splitting (ZFS) in the material. These effects are not accounted for in Kim et al.'s spin-only expression for $\Phi(T)$.[16] The experimental bulk scaling factor computed above is in excellent agreement with the first principles average Φ value obtained with the H20 functional, as shown in Table S3a.

2.4. First principles relaxation of honeycomb-ordered P2-$Na_x[Li_yNi_zMn_{1-y-z}]O_2$ (x,y,z ≤ 1) structures and consequences on spin density transfer pathway geometries

2.4.a. Off-centering of prismatic Na in P2-$Na_x[Li_yNi_zMn_{1-y-z}]O_2$ (x,y,z ≤ 1)

Structural relaxation results in off-centering of Na^+ ions in trigonal prismatic sites in P2-$Na_x[Li_yNi_zMn_{1-y-z}]O_2$ materials. This phenomenon is thought to arise from uncompensated electrostatic repulsions[22] and has been reported in P2-$Na_{0.6}Cr_{0.6}Ti_{0.4}O_2$,[22] P2-$Na_xCoO_2$,[23,24] and P2-$Na_{5/6}Li_{1/4}Mn_{3/4}O_2$[25].

Since the magnitude and sign of individual BPCs is very sensitive to geometry,[17] off-centering of Na^+ ions in P(2d) sites, e.g. in P2-$Na_{2/3}Ni_{1/3}Mn_{2/3}O_2$, leads to Mn^{4+}-O-Na BPCs, for Mn in position M relative to the central Na, ranging from 403 to 632 ppm for H20 calculations, and from 351 to 550 ppm for H35 calculations. Ni^{2+}-O-Na BPCs, for Ni in position M' relative to the central Na, range from 226 to 295 ppm for H20 calculations, and from 280 to 372 ppm for H35 calculations. The BPCs presented in Figure 5 are averages over the different values obtained for a given pathway type.

2.4.b. Distortion of LiO_6 octahedra in the TM layers

First principles TM-O-Li BPCs for Li in an O_h TM layer site in P2-$Na_{0.83}Li_{0.16}Ni_{0.16}Mn_{0.67}O_2$ are presented in Table S4. For Li in an O_h TM layer site interacting with Mn, unpaired spin density is delocalized from the half-filled t_{2g} orbital on Mn^{4+} (d^3) to the Li s orbital via two approximately 90° Li-O-Mn superexchange pathways, giving rise to a positive shift. In addition, direct overlap between the half-filled Mn t_{2g} orbital and the Li s orbital leads to a positive shift and is highly sensitive to small changes in the Mn-Li distance. As expected, the range of Mn-O-Li bond pathway geometries observed in the structure results in significant variation in the BPCs presented in Table S4. The magnitude of the Li-O-Mn BPC is more sensitive to bond distance than to bond angle.

In the case of Ni^{2+} (d^8), t_{2g} orbitals are filled and e_g orbitals are half-filled. An ideal 90° $Ni^{2+}(t_{2g})$-O(p)-Li polarization pathway is much weaker than the 90° delocalization type

mechanism discussed in the case of Mn^{4+} and leads to the transfer of negative spin density onto the Li nucleus. The computed Ni BPCs are indeed small and negative. We note that any deviation from the ideal 90° geometry and from the ideal case where all t_{2g} orbitals are filled and e_g orbitals are half-filled will affect the magnitude and sign of spin density transfer. We believe that such deviations account for the small positive experimental BPC of 18±14 ppm obtained for P2-$Na_{0.8}Li_{0.12}Ni_{0.22}Mn_{0.66}O_2$.

TM	δ (H20) / ppm	δ (H35) / ppm	d(Li-Mn) and Li-O-Mn angles
Mn^{4+}	199	165	2.89 Å, 91.9 and 93.5 °
	269	228	2.88 Å, 91.9 and 93.5°
	334	290	2.84 Å, 93.0 and 93.4°
	331	296	2.81 Å, 2x92.0°
	345	315	2.83 Å, 2x93.0°
Ni^{2+}	-24	-37	2.83 Å, 85.8 and 88.3°
	-24	-38	2.79 Å, 86.6 and 87.8°

Table S4. First principles Mn^{4+}-O-Li and Ni^{2+}-O-Li BPCs computed for Li in an O_h TM layer site in P2-$Na_{0.83}Li_{0.16}Ni_{0.16}Mn_{0.67}O_2$. The Mn^{4+}-O-Li and Ni^{2+}-O-Li BPCs were scaled using the Ni and Mn site-specific scaling factors presented in Table S3c.

2.5. Li shifts for O_h sites in O2 layers

Total Li isotropic shifts for selected O_h environments in the Na layers of a hypothetical honeycomb ordered O2-$Na_x[Li_yNi_zMn_{1-y-z}]O_2$ structure, computed using BPCs shown in Figure 10 in the main text, are presented in Table S5.

Face sharing		Edge sharing		δ_{iso} (H20) / ppm	δ_{iso} (H35) / ppm
M	M’	M	M’		
Mn	3 Mn, 2 Ni, 1 Li	2 Mn, 1 Ni	2 Mn, 1 Li	441	386
Mn	3 Mn, 1 Ni, 2 Li	2 Mn, 1 Ni	2 Mn, 1 Li	418	358
Mn	3 Mn, 2 Ni, 1 Li	2 Mn, 1 Li	2 Mn, 1 Ni	538	510
Mn	3 Mn, 1 Ni, 2 Li	2 Mn, 1 Li	2 Mn, 1 Ni	514	482
Li	6 Mn	2 Mn, 1 Li	2 Mn, 1 Li	459	407
Li	6 Mn	2 Mn, 1 Ni	2 Mn, 1 Ni	542	515

Li	6 Mn	2 Mn, 1 Li	2 Mn, 1 Ni	549	523
Li	6 Mn	2 Mn, 1 Ni	2 Mn, 1 Li	453	399

Table S5. Total isotropic shifts (δ_{iso}), for Li in selected O_h Na sites in an O2 honeycomb-ordered structure, computed from the HYB20 and HYB35 BPCs shown in Figure 10 in the main text. Of note, O_h environments face-sharing with a Ni in an adjacent TM layer were not considered, due to the lack of a first principles calculation for this bond pathway type.

References

1. X. Wu, G.-L. Xu, G. Zhong, Z. Gong, M. J. McDonald, S. Zheng, R. Fu, Z. Chen, K. Amine, and Y. Yang, *ACS Appl Mater Interfaces*, 2016, **8**, 22227–22237.
2. I. Hung, L. Zhou, F. Pourpoint, C. P. Grey, and Z. Gan, *J. Am. Chem. Soc.*, 2012, **134**, 1898–1901.
3. Z. Lu and J. R. Dahn, *Chem. Mater.*, 2001, **13**, 1252–1257.
4. J. Xu, D. H. Lee, R. J. Clément, X. Yu, M. Leskes, A. J. Pell, G. Pintacuda, X.-Q. Yang, C. P. Grey, and Y. S. Meng, *Chem. Mater.*, 2014, **26**, 1260–1269.
5. D. Buchholz, L. G. Chagas, C. Vaalma, L. Wu, and S. Passerini, *J. Mater. Chem. A*, 2014, **2**, 13415.
6. A. Caballero, L. Hernán, J. Morales, L. Sánchez, J. S. Peña, and M. A. G. Aranda, *J. Mater. Chem.*, 2002, **12**, 1142–1147.
7. A. D. Becke, *J. Chem. Phys.*, 1993, **98**, 5648–5652.
8. C. Lee, W. Yang, and R. Parr, *Phys. Rev., B Condens. Matter*, 1988, **37**, 785–789.
9. S. H. Vosko, L. Wilk, and M. Nusair, *Can. J. Phys.*, 1980, **58**, 1200–1211.
10. P. J. Stephens, F. J. Devlin, C. F. Chabalowski, and M. J. Frisch, *J. Phys. Chem.*, 1994, **98**, 11623–11627.
11. F. Corà, M. Alfredsson, G. Mallia, D. S. Middlemiss, W. C. Mackrodt, R. Dovesi, and R. Orlando, in *Principles and Applications of Density Functional Theory in Inorganic Chemistry II, Structure and Bonding 113,* ed. N. Kaltsoyannis, J. E. McGrady,

Springer, Berlin/Heidelberg, 2004, Chapter 5, pp. 171–232.

12. J. Muscat, A. Wander, and N. M. Harrison, *Chem. Phys. Lett.*, 2001, **342**, 397–401.
13. X. Feng and N. Harrison, *Phys. Rev. B*, 2004, **70**, 092402.
14. D. S. Middlemiss, L. M. Lawton, and C. C. Wilson, *J. Phys.: Condens. Matter*, 2008, **20**, 335231.
15. I. de P R Moreira, F. Illas, and R. Martin, *Phys. Rev. B*, 2002, **65**, 155102.
16. J. Kim, D. S. Middlemiss, N. A. Chernova, B. Y. X. Zhu, C. Masquelier, and C. P. Grey, *J. Am. Chem. Soc.*, 2010, **132**, 16825–16840.
17. D. S. Middlemiss, A. J. Ilott, R. J. Clément, F. C. Strobridge, and C. P. Grey, *Chem. Mater.*, 2013, **25**, 1723–1734.
18. R. J. Clément, A. J. Pell, D. S. Middlemiss, F. C. Strobridge, J. K. Miller, M. S. Whittingham, L. Emsley, C. P. Grey, and G. Pintacuda, *J. Am. Chem. Soc.*, 2012, **134**, 17178–17185.
19. R. Dovesi, V. R. Saunders, C. Roetti, R. Orlando, C. M. Zicovich-Wilson, B. Civalleri, F. Pascale, K. Doll, N. M. Harrison, I. J. Bush, P. DArco, and M. Llunell, *Crystal09 user's manual*, University of Torino: Torino, Italy, 2010.
20. A. Schäfer, H. Horn, and R. Ahlrichs, *J. Chem. Phys.*, 1992, **97**, 2571–2577.
21. H. J. Monkhorst and J. D. Pack, *Phys. Rev. B*, 1976, **13**, 5188.
22. Y. Wang, R. Xiao, Y.-S. Hu, M. Avdeev, and L. Chen, *Nat. Commun.*, 2015, **6**, 6954.
23. J. D. Jorgensen, M. Avdeev, D. G. Hinks, J. C. Burley, and S. Short, *Phys. Rev., B Condens. Matter*, 2003, **68**, 214517.
24. L. Viciu, Q. Huang, and R. J. Cava, *Phys. Rev. B*, 2006, **73**, 212107.
25. N. Yabuuchi, R. Hara, M. Kajiyama, K. Kubota, T. Ishigaki, A. Hoshikawa, and S. Komaba, *Adv. Energy Mater.*, 2014, **4**, 1301453.